Research Article | Vol. 32, No. 8 / 8 Apr 2024 / *Optics Express* 14685

Optics EXPRESS

Femtosecond laser writing of fiber Bragg gratings using the phase mask technique: a geometrical optics analysis based on the Bravais refractive index

CYRIL HNATOVSKY AND STEPHEN J. MIHAILOV*

National Research Council Canada, 100 Sussex Drive, Ottawa, ON, K1A 0R6, Canada
**Stephen.Mihailov@nrc-cnrc.gc.ca*

Abstract: Material modification is produced inside silica-based optical fibers of different diameters using tightly focused near-infrared (central wavelength at 800 nm) femtosecond laser pulses and the phase mask technique which is often employed for laser inscription of fiber Bragg gratings. 1^{st}-, 2^{nd}-, and 3^{rd}-order phase masks designed for the operation at 800 nm are used in the experiments. The inscription is performed at different distances from the fiber's front surface by translating the focusing cylindrical lens along the laser beam propagation direction. The results show that the material modification produced by means of the 2^{nd}- and 3^{rd}-order phase mask can be positioned at any predetermined distance from the fiber's front surface. In contrast, when the 1^{st}-order mask is used for laser writing, the maximum distance from the fiber's front surface at which material modification can be produced is limited and determined by three main parameters: the diffraction angle of the phase mask, the refractive index of the fiber and the diameter of the fiber.

1. Introduction

There are two principal methods to inscribe fiber Bragg gratings (FBG) with laser light. The first method is performed (i) by simultaneously irradiating a length of the fiber with an interference pattern that is generated by an amplitude-splitting/wavefront-splitting free space interferometer or a phase mask (i.e., a transmission diffraction grating) [1–5], or (ii) by using point-by-point [6,7], line-by-line [8,9], or plane-by-plane [10] writing techniques when the laser beam induces changes in the fiber core in a sequential fashion. Each of the above two general methods has its own advantages and limitations, as discussed in the extensive literature on this subject matter [1,2,11,12].

The phase mask technique (the PM-technique) is typically used with i) a continuous-wave or nanosecond ultraviolet laser (i.e., excimer lasers) [1,2] or ii) a femtosecond (FS) laser [4,5]. The latter option is highly advantageous for some applications as it does not require any photosensitization of the fiber core [13]. Additionally, infrared FS lasers can also inscribe FBGs through transparent and semi-transparent protective coatings if the pulses are tightly focused [14–17].

The classical optical setup utilizing a phase mask, which consists of a focusing cylindrical lens, a phase mask and a fiber inside which an FBG is to be inscribed, is deceptively simple [4]. In reality, when considering inscription with a FS laser, one has to take into account: i) the bandwidth, chirp and polarization of the ultrashort pulses, ii) aberrations (chromatic and spherical) of the focusing cylindrical lens [18], iii) aberrations (spherical aberration, chromatic dispersion, conical diffraction) introduced by the phase mask [18], polarization-dependent intensity distribution after the phase mask [19], walk-off effects introduced by the phase mask [18,20,21], and iv) focusing and distortion of the laser pulses by the fiber itself.

#520723
Journal © 2024

https://doi.org/10.1364/OE.520723
Received 1 Feb 2024; revised 18 Mar 2024; accepted 19 Mar 2024; published 4 Apr 2024

The "fiber effect" cannot be disregarded. The small diameter of an optical fiber makes it a strong rod lens and, as a consequence, the shape and size of the laser focus produced behind the phase mask are expected to be quite different when observed in free space and inside the fiber. Despite the fact that the PM-technique has been used for decades, the focusing effect introduced by the fiber was considered only for the case when the phase mask is actually removed from the optical path [22]. In practice, the phase mask diffracts the laser beam into several diffraction orders and the angled incidence of the diffracted beams onto the fiber's surface needs to be taken into account, especially when considering the tight focusing geometries used during through-the-coating FS laser inscription with a phase mask.

In this work we demonstrate that when the phase mask diffracts an incident FS beam at large angle, material modification can be formed inside the fiber only up to a certain distance from the fiber's front surface, even if the cylindrical lens focuses the beam tightly. In fact, our results show that FBG inscription in multi-core or large-core fibers [23–29] using small-period 1st-order phase masks (i.e., large diffraction angle) may be physically impossible if the fiber is irradiated from one side. A 1st-order phase mask is defined to be one where the generated interference pattern produces a fundamental or 1st-order Bragg resonance in the fiber. Higher order masks produce higher order Bragg resonances in the fiber [4]. For a phase mask that uses 800 nm FS laser light to produce a grating with a 1st-order Bragg resonance at the 1550 nm telecom wavelength, the diffraction angle of the ±1 diffraction order is ≈48° [4]. We also demonstrate that the above constraint of limited penetration distance of material modification is removed if higher-order phase masks (i.e., phase masks with larger periods and smaller diffraction angles) are used instead. To understand these results, we propose to employ a formalism that is based on the Bravais effective refractive index for the cylinder [30–33]. Even though this formalism was originally developed for the studies of the interior and exterior caustics produced by diagonally incident plane waves refracted by cylindrical objects, we show that it can also be applied to tilted focused laser beams and thus be used to model FBG inscription using the PM-technique within a wide range of experimental conditions.

2. Background

Light propagation in the optical setup is analyzed using geometrical optics in the paraxial approximation. This simple formalism is insightful and also quite accurately describes the experimental data.

2.1. Optical setup

Figures 1(a) and 1(b) respectively show the top and side views of the most basic FBG-inscription setup based on the PM-technique. Consider a spatially non-chirped and non-tilted FS pulse [34–36] falling normally onto a phase mask (M in Figs. 1(a) and 1(b)). The pulse front (i.e., the intensity front) is assumed to be parallel to the mask. After the interaction of the pulse with M, a set of diffracted pulses that propagate along different directions is formed. The phase fronts of the resulting diffracted pulses are normal to their propagation direction, whereas their pulse fronts remain parallel to M. This implies that the diffracted pulses, except for those in the 0 diffraction order, have become tilted, angularly dispersed and spatially chirped pulses. The combination of angular dispersion and spatial chirp make the average wavelength of the pulse vary along the pulse front. If the spectral profile of the FS pulse is symmetric with respect to the central wavelength, the maximum intensity in the pulse front occurs at its center. At this point, we assume that M generates only 0 and ±1 diffraction orders, i.e., it is a 1st-order mask.

When both the focusing cylindrical lens (L in Figs. 1(a) and 1(b)) and M are placed at a right angle to the incident FS beam, L focuses the diffracted pulses into focal lines that remain parallel to M. The axis of L should be perpendicular to the grooves on M to ensure that the focal lines of the ±1 diffraction orders overlap along the y-axis [37].

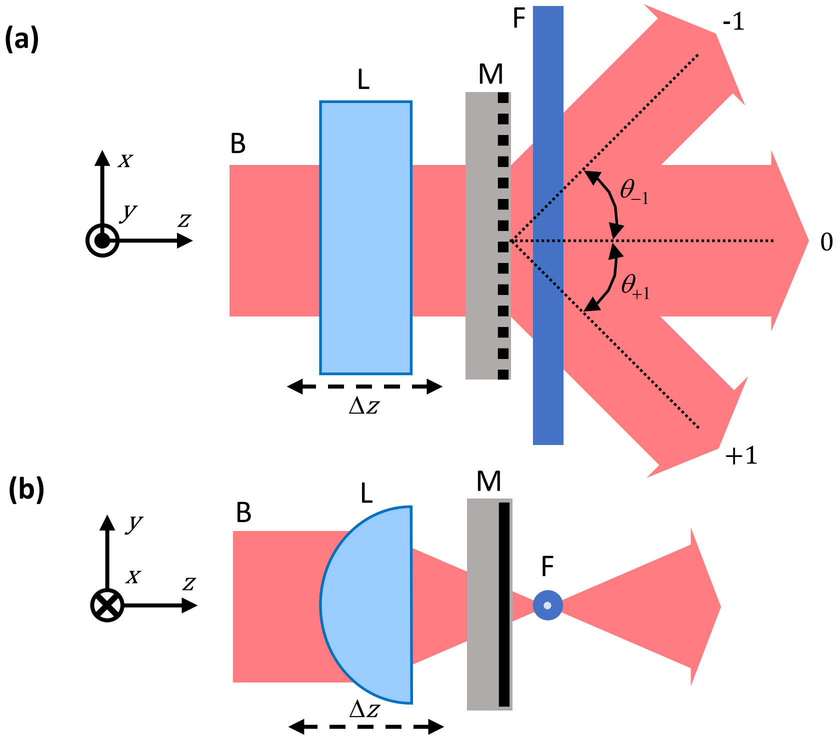

Fig. 1. A schematic of the classical laser-writing optical setup based on the PM-technique. (a) Top view. B, L, M and F denote the FS beam, the focusing cylindrical lens, the phase mask and the optical fiber, respectively. M splits B into 0 and ±1 diffraction orders. The diffraction angles of the ±1 diffraction orders are θ_{+1} and θ_{-1}, respectively. F is placed where the ±1 diffraction orders overlap and form an interference pattern that is used for the inscription. (b) Side view. B is focused inside F. The line-shaped laser focus, which is formed by the overlapping focal lines of the ±1 diffraction orders and aligned along the fiber, can be moved inside F by translating L along the z-axis by Δz. L and F and are aligned along the x-axis. M lies in the xy-plane and the grooves on M are parallel to the y-axis.

2.2. Alignment procedure

In reference to Fig. 1, the fiber axis is placed a few hundred micrometers (μm) behind the focal plane of L. F acts as a strong cylindrical rod lens and forms images of the focal lines corresponding to different diffraction orders produced by M. Figure 2(a) displays the situation when only 0 and ±1 diffraction orders are formed by M. When M and L are positioned at a right angle with respect to the axis of beam B (see captions to Figs. 1(a) and 1(b)), the diffraction angles of the ±1 diffraction orders, i.e., θ_{+1} and θ_{-1} in Figs. 1(a) and 2(a), are the same and given by $\theta_{+1} = \theta_{-1} = \theta_1 \equiv \sin^{-1}\lambda/\Lambda$, where λ is the wavelength of the incident light and Λ is the period of M. F is then moved along the z-axis towards L (the positions of M and L are fixed in space) until the front focal plane of F (Fig. 2(b)) is placed at the focal lines (FL in Fig. 2(a)) of the ±1 diffraction orders. In this case, the images of the focal lines of the ±1 diffraction orders are formed by F at infinity in the geometrical optics approximation. If the positions of M and F are fixed in space, the alignment is performed by moving L along the z-axis towards F until the focal lines of the ±1 diffraction orders are placed at the front focal plane of F. We note that when L is translated by Δz along the z-axis, the focal line of the 0 diffraction order also moves by Δz, whereas the overlapping focal lines of the ±1 diffraction orders move by $\Delta z \cos\theta_1$.

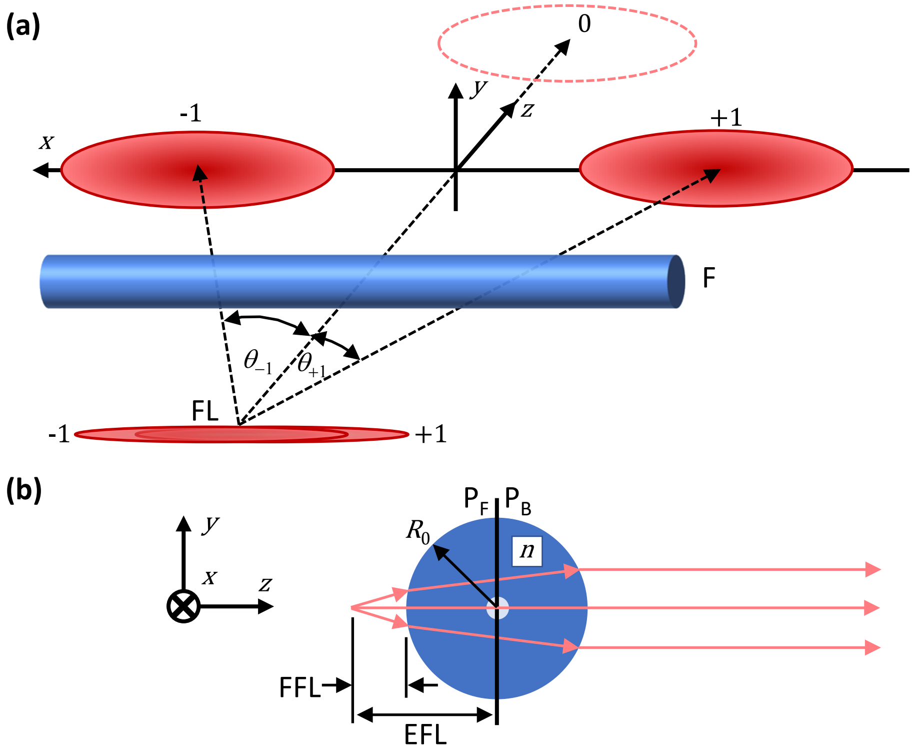

Fig. 2. A schematic of the fiber alignment procedure wherein the fiber acts as a rod lens. (a) Formation of far-zone images of the focal lines (FLs) corresponding to ±1 diffraction orders. The FLs, which become angularly dispersed and spatially chirped after M, fully overlap along the *y*-axis and the *z*-axis, but only partially overlap along the *x*-axis due to the lateral walk-off of the −1 and +1 diffraction orders [21]. The focusing cylindrical lens and the phase mask (L and M in Figs. 1(a) and 1(b), respectively) are not shown for clarity. (b) Defining the effective focal length (EFL) and the front focal length (FFL) of a rod lens (i.e., F) in air. EFL is the distance from the front focal plane of the rod lens to its front principal plane (P_F). FFL is the distance from the front focal plane of the rod lens to its front surface. For a rod lens, P_F coincides with the back principal plane (P_B). P_F and P_B lie in the *xy*-plane that intersects the axis of the rod lens. The radius and the refractive index of the rod lens are denoted by R_0 and n, respectively.

The angular position of F with respect to the focal lines is adjusted by monitoring their images, for instance, by means of a detector card (Fig. 2(a)). When the fiber axis and the focal lines are aligned, the images of the focal lines of the ±1 diffraction orders lie in the same *xz*-plane and look symmetric in the *xy*-plane.

Figure 2(b) depicts F as a rod lens of refractive index n and radius R_0 and defines its effective focal length (EFL) and front focal length (FFL). When the axis of the incident light beam is at a right angle with respect to the axis of the rod lens, EFL is given in the paraxial approximation by

$$\mathrm{EFL} = \frac{R_0 n}{2(n-1)} \tag{1}$$

and FFL (i.e., EFL-R_0) is given by

$$\mathrm{FFL} = \frac{R_0(2-n)}{2(n-1)} \tag{1a}$$

2.3. Refraction at the fiber's front surface

Consider a convex circular cylindrical boundary of radius R_0 between two regions with refractive indices 1 and n (Fig. 3(a)). This boundary represents the front surface of F. The origin of the coordinate system coincides with the intersection point of the boundary and the z-axis (Fig. 3(a)). This also implies that the value of the z-coordinate of L is negative.

1) We will first analyze the case when i) M is removed from the beam path or ii) M produces 0 and ±1 diffraction orders but only the 0 diffraction order is considered. In this scenario, the source (or the object) is the line-shaped focus formed by L and the image is formed by the cylindrical boundary.

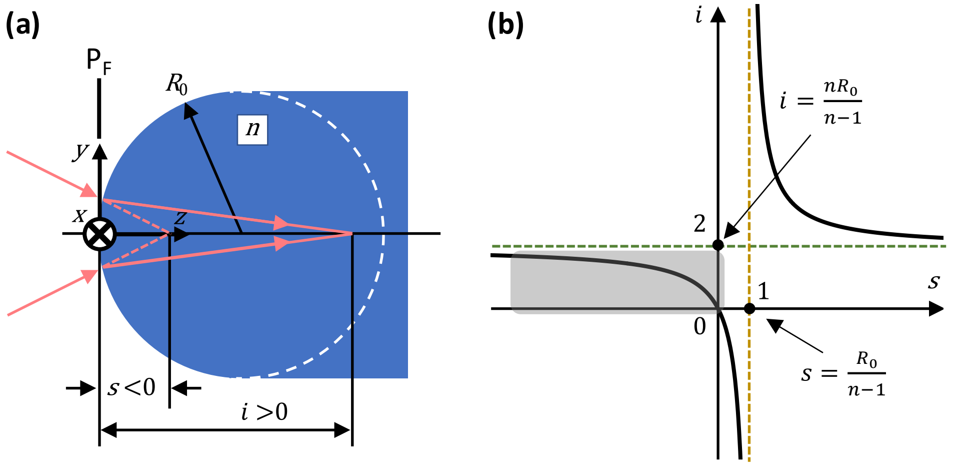

Fig. 3. Finding the image of a line-shaped source after refraction at a convex cylindrical boundary of radius R_0. The boundary separates two media with refractive indices 1 (air) and n (fiber material). (a) Defining the source and its image that is formed by the cylindrical boundary. The incident rays are perpendicular to the generatrix of the boundary. The front principal plane (P_F) of the boundary is at $z = 0$. (b) A schematic plot of Eq. (2) where the image distance i is presented as a function of the source distance s.

Both L and F are aligned along the x-axis (Fig. 3(a)). In the paraxial approximation, the positions of the source and its image are defined by the following equation:

$$\frac{1}{s}+\frac{n}{i}=\frac{n-1}{R_0}, \tag{2}$$

where s and i respectively denote the distance of the source and the image from the boundary. Equation (2) can be derived from Abbe's invariant for an air-glass cylindrical boundary, $1/R_0 - 1/s = n(1/R_0 - 1/i)$, provided that the following sign conventions are used. Distance s is positive when the source is on the left-hand side of the boundary (i.e., in front of F) and is negative when the source is on the right-hand side of the boundary (i.e., inside F). Distance i is positive when the image is formed on the right-hand side of the boundary (i.e., inside F) and is negative when the image is formed on the left-hand side of the boundary (i.e., in front of F). R_0 is positive as the center of curvature of the cylindrical boundary is on its right-hand side.

A schematic plot of Eq. (2) is presented in Fig. 3(b). In the context of this work, we are interested in the shaded region of the plot. The vertical asymptote intersects the s-axis at point 1 and defines the front EFL of the boundary, (i.e., $R_0/(n-1)$). The horizontal asymptote intersects the i-axis at point 2 and defines the distance (i.e., $nR_0/(n-1)$) at which parallel rays propagating along the z-axis are focused by the boundary inside the medium with refractive index n (i.e., fiber material). As an example, the boundary will focus parallel incident rays propagating along the z-axis at $i = 3R_0$ for $n = 1.5$ and at $i \leq 2R_0$ for $n \geq 2$, which implies that for silica-based optical fibers with $n \approx 1.45$ for near-infrared wavelengths such rays cannot be focused within the fiber.

2) M produces 0 and ±1 diffraction orders, but only the ±1 diffraction orders are considered in terms of their focusing by F. The overlapping focal lines of the ±1 diffraction orders (FL in Fig. 2(a)) represent the sources whose images are formed by the cylindrical boundary. As before, the focal lines and F are aligned along the x-axis. Due to the fact that the diffracted light (i.e., the phase fronts of the FS pulses) impinges F at an angle (i.e., θ_1), we propose to introduce two changes into Eq. (2). Firstly, we replace s with $s\cos\theta_1$. The $\cos\theta_1$-factor takes into account the fact that the plane of observation is the yz-plane, whereas the incident rays forming the source lie in the plane that contains the y-axis and is at an angle θ_1 with respect to the yz-plane. To be precise, the image distance i is measured from the origin of the xyz-coordinate system along the z-axis, whereas the source distance s is measured from the origin of a different, $\tilde{x}\tilde{y}\tilde{z}$-coordinate system along the $\tilde{z}$-axis. The origins of the xyz-coordinate system and $\tilde{x}\tilde{y}\tilde{z}$-coordinate system coincide, the $\tilde{y}$-axis is aligned along the y-axis, and the $\tilde{z}$-axis is at an angle θ_1 with respect to the z-axis. Secondly, we replace the conventional refractive index n with the Bravais effective refractive index for the cylinder $n_B(\theta_1)$ [30–33].

The Bravais refractive index is often used in atmospheric optics to calculate the propagation of diagonally incident rays through prismatic ice crystals. It was shown in Ref. [30] that the Bravais-index formalism also applies to diagonally illuminated long circular dielectric cylinders. According to Refs. [31,32], $n_B(\theta_1)$ is given by

$$n_B(\theta_1) = \frac{\sqrt{n^2 - \sin^2\theta_1}}{\cos\theta_1} \tag{3}$$

By introducing the above changes to Eq. (2), we arrive at

$$\frac{1}{s\cos\theta_1} + \frac{n_B(\theta_1)}{i} = \frac{n_B(\theta_1) - 1}{R_0} \tag{4}$$

We also note that in the case of diagonal illumination, the ordinary refractive index n of the fiber in Eqs. (1) and (1a) becomes the Bravais refractive index $n_B(\theta_1)$. The dependence of $n_B(\theta_1)$ on the illumination angle θ_1 is quite strong, as it can be seen from the following examples. For silica-based optical fibers with $n \approx 1.45$ for near-infrared wavelengths, $n_B(\theta_1)$ is approximately equal to 1.50, 1.70 and 2.33 if θ_1 is 20°, 40° 60°, respectively. Importantly, a focus can now be formed within the fiber with $n \approx 1.45$ in parallel incident rays if $n_B(\theta_1) \geq 2$ [30], which corresponds to $\theta_1 \geq 53°$.

In this work we assume that the refractive index of the fiber, n, is uniform because the refractive indices of the cladding(s) and the core(s) are typically very close to one another. If the refractive index of the core(s) is much higher than that of the cladding(s) but the core diameter is much smaller than the cladding diameter, the analysis based on a single refractive index, n, remains valid because the light propagation occurs predominantly in the cladding. The analysis of the case when the core diameter is large and the refractive index mismatch between the core(s) and the cladding(s) is large goes beyond the scope of this work.

For the purposes of this work, it is more convenient to express $n_B(\theta_1)$ and $\cos\theta_1$ in terms of λ and Λ as these variables are the main parameters that describe the phase mask and its diffraction properties. Namely,

$$\cos\theta_1 = \sqrt{1 - \left(\frac{\lambda}{\Lambda}\right)^2}; \; n_B(\theta_1) = \sqrt{\frac{(n\Lambda)^2 - \lambda^2}{\Lambda^2 - \lambda^2}} \tag{5}$$

3. Experimental results

In our experiments, we used the classical optical setup for the PM-technique (Figs. 1(a) and 1(b)) [4] and a Ti-sapphire regeneratively amplified laser system operating at a central wavelength λ of 800 nm. The Fourier-transform-limited pulse duration of the FS laser was 80 fs and the pulse repetition rate was 1 kHz.

In the first set of experiments, the linearly polarized output FS laser beam (B; 7 mm in diameter at the $1/e^2$-intensity level) was focused into silica-based optical fibers (F) of different diameters ($2R_0$ = 80 µm, 125 µm (SMF-28), and 400 µm) either without a phase mask (M) in the optical path or using a 1st-order holographic phase mask (Ibsen Photonics A/S) with a period $\Lambda^{(1)}$ of 1.07 µm ($\theta_1^{(1)} = \sin^{-1}\lambda/\Lambda^{(1)}$), where the superscripted "1" refers to the order of the phase mask. The two-beam interference pattern generated by the ±1 diffraction orders of this mask would produce an FBG with a fundamental or 1st-order Bragg resonance. It should be noted that in the experiments without a phase mask the output FS beam was in fact focused through the 2.1 mm-thick substrate of the 1st-order mask without intercepting the mask grooves.

In the second set of experiments, a 2nd- or 3rd-order phase mask ($\Lambda^{(2)}$ = 2.14 µm and $\Lambda^{(3)}$ = 3.21 µm), manufactured using electron beam lithography on a 3.4 mm-thick substrate, was inserted in the optical path to study in more detail the effect of the respective diffraction angles (i.e., $\theta_1^{(2)} = \sin^{-1}\lambda/\Lambda^{(2)}$ and $\theta_1^{(3)} = \sin^{-1}\lambda/\Lambda^{(3)}$) on the inscription process. As before, the superscripted "2" and "3" refer to the order of the phase masks. The two-beam interference pattern generated by the ±1 diffraction orders of these mask would produce FBGs with a 2nd- and 3rd-order Bragg resonances, respectively. Only the 125 µm-diameter fiber was tested in this case.

When the phase masks were used, the FS laser beam was expanded ~3.5 times along the x-axis (i.e., the fiber axis) using a cylindrical telescope to minimize the lateral walk-off effect of the +1 and −1 diffraction orders [21], which is essential in the case of the 1st-order mask.

The beam was focused using a plano-convex cylindrical lens (L) corrected for spherical aberration. Nominally, a complete correction can be achieved if the curved surface of L is facing the furthest conjugate point, i.e., the incident collimated FS laser beam (see Fig. 1(b) and the insets of Figs. 7(a) and 7(b)). The focal length of L was 15 mm and the effective numerical aperture (NA) of L was estimated to be 0.23. The focal lines of the 0 and ±1 diffraction orders were placed 300 µm behind the back surfaces of the phase masks by adjusting the position of L. The front surfaces of the fibers (protective coating removed) were placed 350-400 µm away from the phase mask.

For alignment, the optical fiber was moved along the z-axis until the focal lines of the 0 or ±1 diffraction orders were placed at its front focal plane and the sharpest images of the focal lines were formed a few centimeters away from F (see Fig. 2(a)). Then, L was translated a certain distance D_{R_0} further along the positive direction of the z-axis until the focal lines were placed in the fiber core. The respective z-coordinate of L is denoted by z_{R_0}. The alignment of the overlapping focal lines with respect to the fiber core was performed using nonlinear photoluminescence microscopy, as described in Ref. [38]. For each fiber-mask combination tested, this distance (i.e., D_{R_0}) was measured several times and averaged. We note that the situation when the image is in the fiber core corresponds to $i = R_0$ in Eqs. (2) and (4). The respective value of s is $-R_0$ (denoted by s_{R_0}) if there is no phase mask in the optical beam path (see Eq. (2)) and

$$s_{R_0} = \frac{-R_0\Lambda}{\sqrt{\Lambda^2 - \lambda^2}} \tag{6}$$

if a phase mask with a period of Λ is inserted into the beam (see Eq. (4)). Distance D_{R_0} is given by Eq. (1) without a phase mask in the beam path (FFL + $|s_{R_0}| = R_0(2-n)/[2(n-1)] + R_0 =$

$R_0 n/[2(n-1)]$) and, according to Eqs. (1a), (3) and (6), by

$$D_{R_0} = \text{FFL} + |s_{R_0}| = R_0 \left[\frac{2 - \sqrt{\frac{(n\Lambda)^2-\lambda^2}{\Lambda^2-\lambda^2}}}{2\left(\sqrt{\frac{(n\Lambda)^2-\lambda^2}{\Lambda^2-\lambda^2}} - 1\right)} + \frac{\Lambda}{\sqrt{\Lambda^2-\lambda^2}} \right] \tag{7}$$

if there is a phase mask in the beam path. In Eq. (7), FFL is measured in the plane that contains the y-axis and is at an angle θ_1 with respect to the yz-plane.

For each fiber under consideration, the laser-inscription was conducted at different values of the z-coordinate of L ($|z'_l|>|z'_{l-1}|>\ldots>|z'_1|>|z_{R_0}|>|z_1|>\ldots>|z_{m-1}|>|z_m|$) which correspond to different values of $|s|$ ($|s'_l|<|s'_{l-1}|<\ldots<|s'_1|<|s_{R_0}|<|s_1|<\ldots<|s_{m-1}|<|s_m|$), where $|s|$ and $|z|$ denote the absolute values of the negative distances s and z. Indeed, the z-coordinate of L is nominally negative because L is on the left-hand side of the air-fiber boundary (i.e., in front of F; Fig. 3(a)). In order to avoid any possible confusion, we would like to emphasize that z is the physical coordinate of L in the coordinate system introduced in Fig. 3(a), whereas the position of the line-shaped focus formed by L (i.e., s) obeys the sign conventions associated with Eq. (2) and Eq. (4). For both Eq. (2) and Eq. (4), $|\Delta z| = |\Delta s|$ (e.g., $|z_{R_0} - z'_l| = |s_{R_0} - s'_l|$). The plots in Figs. 4(b), 5(b-d) and 6(b), which compare the experimental data to the pertinent simulations based on Eq. (4), are presented in the $i(s)$-form in order to be consistent with the notations of Eq. (4). However, as it was mentioned earlier, the quantity we measure in our experiments is the z-coordinate of L (i.e., z) rather than s, which is measured from the origin of the $\tilde{x}\tilde{y}\tilde{z}$-coordinate system along the $\tilde{z}$-axis. What is important is that s is uniquely defined by z and $|\Delta z| = |\Delta s|$.

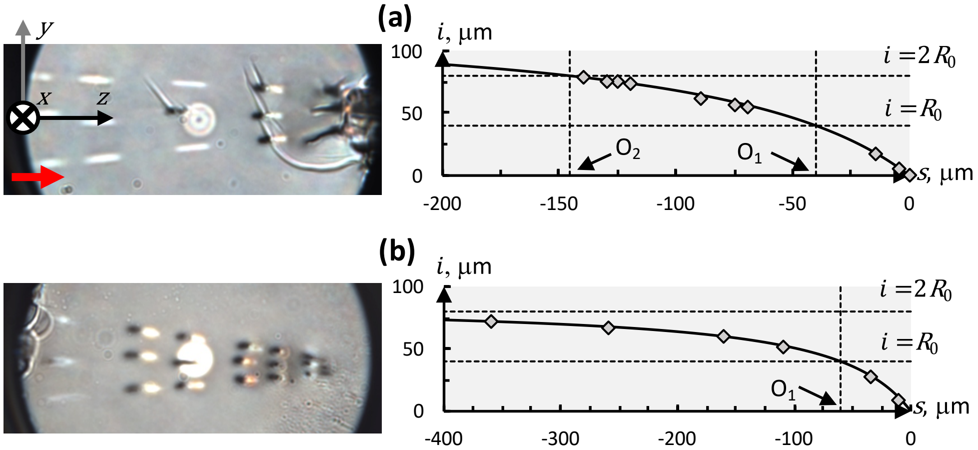

Fig. 4. Laser-inscription in the 80 µm-diameter fiber at different locations. (a) Inscription without a phase mask. (b) Inscription using a 1st-order phase mask with a period $\Lambda^{(1)}$of 1.07 µm. According to Eq. (8b), O$_2$ is located at $s_{2R_0} \approx -933$ µm and is not shown. The solid curves in the plots represent the simulated data generated using Eqs. (2) and (4). The FS pulses propagate along the positive direction of the z-axis, as indicated by the red arrow. The upper, central and lower tracks of laser-modified regions in the optical microscopy images were produced when the y-coordinate of L was 10 µm, 0 µm and −10 µm, respectively.

The pulse energy during the inscription was significantly increased compared with that used in the alignment procedure in order to be able to induce easily observable Type II material modification in the fiber core [39,40]. The first inscription step was performed at the smallest absolute value of the z-coordinate of L, i.e., when the distance between L and F was the shortest. The subsequent inscription steps were performed at progressively increasing absolute values of

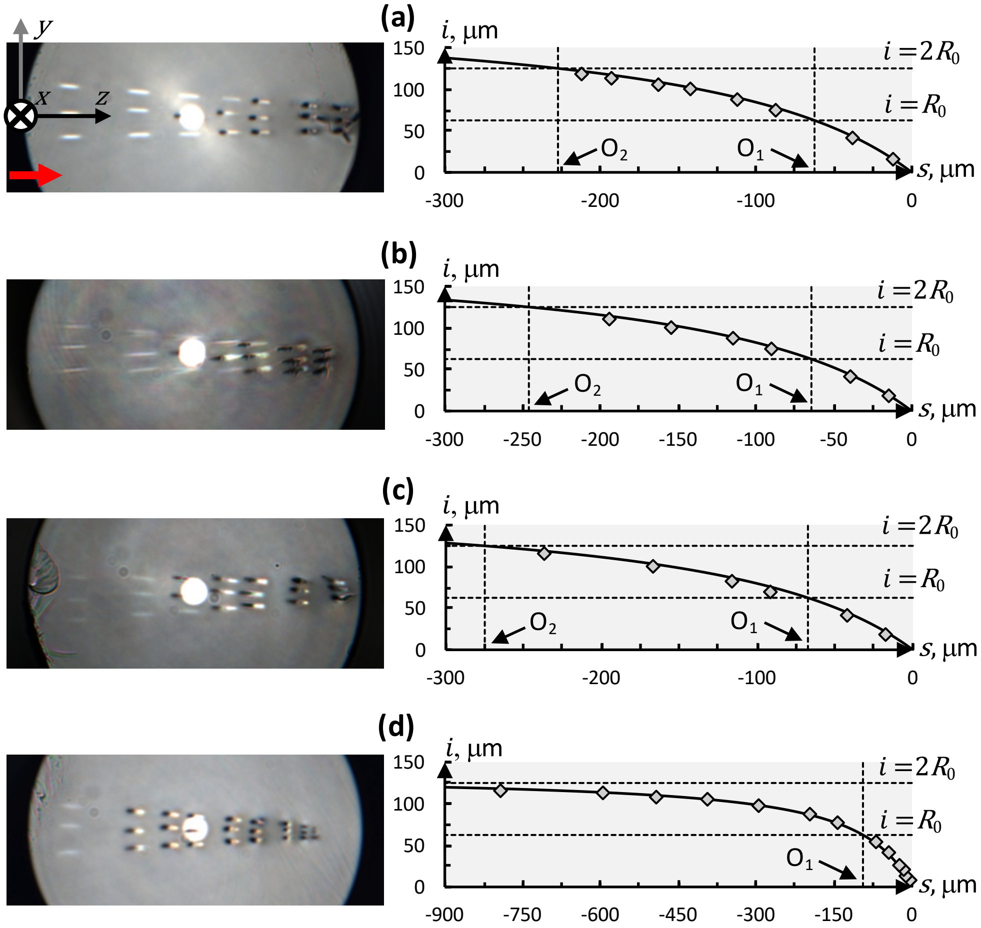

Fig. 5. Laser-inscription in the 125 µm-diameter fiber at different locations. (a) Inscription without a phase mask. (b) Inscription using a 3rd-order phase mask with a period $\Lambda^{(3)}$of 3.21 µm. (c) Inscription using a 2nd-order phase mask with a period $\Lambda^{(2)}$of 2.14 µm. (d) Inscription using a 1st-order phase mask with a period $\Lambda^{(1)}$of 1.07 µm. According to Eq. (8b), O_2 is located at $s_{2R_0} \approx -1457$ µm and is not shown in the plot. The solid curves in the plots represent the simulated data generated using Eqs. (2) and (4). The FS pulses propagate along the positive direction of the z-axis, as indicated by the red arrow. The upper, central and lower tracks of laser-modified regions in the optical microscopy images were produced when the y-coordinate of L was 10 µm, 0 µm and −10 µm, respectively.

the z-coordinates of L, i.e., the distance between L and F was increased by retracting L for each next step and the laser focus was thus moved closer and closer towards the front surface of the fiber. Additionally, during each inscription step, i.e., at a fixed z-coordinate of L, three detached regions were modified, one at a time, across the fiber by changing the position of L along the y-axis by 10 µm. In the experiments presented below (i.e., Figs. 4–6), each modified region received 3×10^3 laser pulses during 3-seconds exposures produced by an electronic shutter. The electronic shutter also blocked the FS beam while L was being moved between the exposures.

To visualize the laser-modified regions inside the fiber and find their positions with respect to the front surface of the fiber, images of the cleaved fiber samples were obtained using optical microscopy in transmitted light. In the optical microscopy images in Figs. 4–6, the light-colored modified regions belong to Type I [39], whereas the dark-colored modified regions belong to

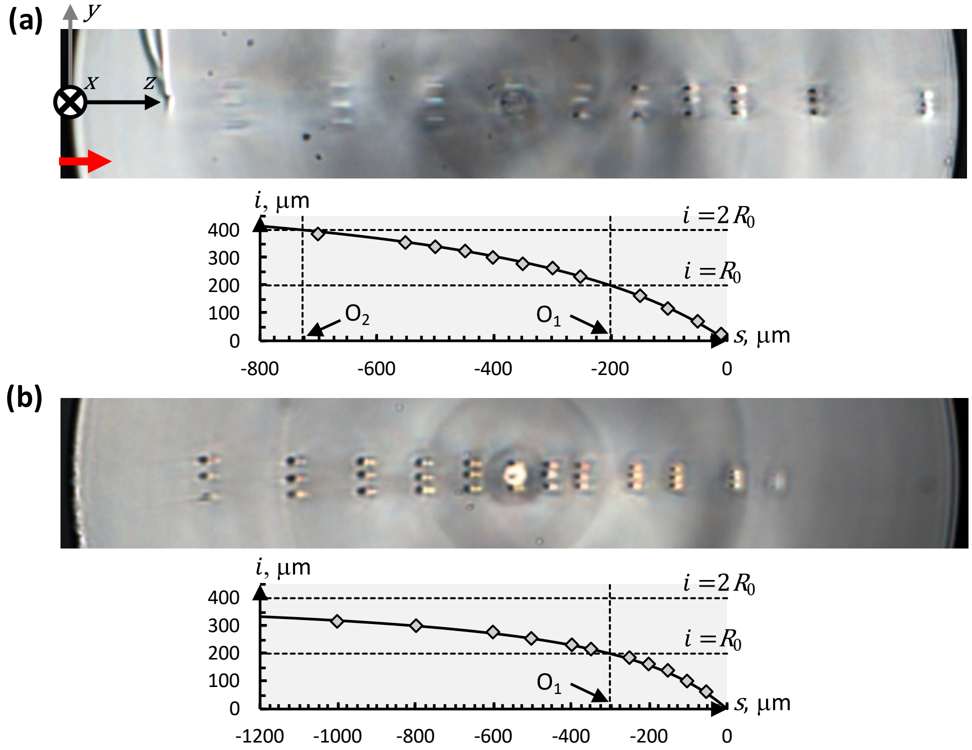

Fig. 6. Laser-inscription in the 400 µm-diameter fiber at different locations. (a) Inscription without a phase mask. (b) Inscription using a 1st-order phase mask with a period $\Lambda^{(1)}$of 1.07 µm. According to Eq. (8b), O_2 is located at $s_{2R_0} \approx -4663$ µm and is not shown in the plot. The solid curves in the plots represent the simulated data generated using Eqs. (2) and (4). The FS pulses propagate along the positive direction of the z-axis, as indicated by the red arrow. The upper, central and lower tracks of laser-modified regions in the optical microscopy images were produced when the y-coordinate of L was 10 µm, 0 µm and −10 µm, respectively.

Type II [39]. Two orthogonal orientations of linear polarization of the FS pulses were used to investigate whether the Type II modification consisted of nanograting structures [40]. When the pulse polarization was aligned along the x-axis, the dark-colored regions in Figs. 4–6 showed up as bright regions if reflection optical microscopy was used for examination, i.e. these regions reflected incident light. On the other hand, when the pulse polarization was aligned along the y-axis, the very same regions did not reflect light and remained dark. Taking into account that light-induced nanograting structures are oriented perpendicularly to the electric vector of the FS pulses, a conclusion was drawn that the laser-modified regions contained stacks of micro-reflectors, that is, nanogratings. Two sets of samples for each fiber-mask combination were prepared using both x-polarization and y-polarization, but only the results of the inscription with one state of polarization, either x-polarization or y-polarization, are presented below.

The centroids of the laser-modified regions represented “images” of the focused FS pulses. The positive image distances $i'_l < i'_{l-1} < \ldots < i_{m-1} < i_m$ corresponding to the source distances $|s'_l| < |s'_{l-1}| < \ldots < |s_{m-1}| < |s_m|$ were measured in order to plot i as a function of s ($i(s)$) and compare the experimental results to the simulations based on Eqs. (2) and (4).

The following subsections summarize our observations.

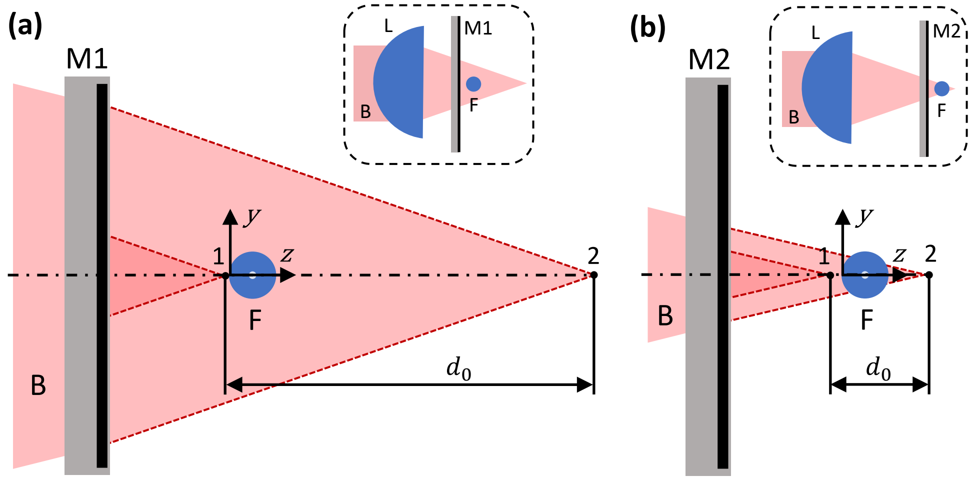

Fig. 7. Visualization of laser-inscription at the back surface of the fiber. (a) and (b) respectively represent inscription using the 1st-order phase mask M1 and the 3rd-order phase mask M2, which are described in the text. A FS beam B is focused through M1 and M2 using the cylindrical lens L with NA = 0.23 described in the text. The mask-to-fiber distance in (a) and (b) is the same, whereas the lens-to-mask distance is smaller in (a) than in (b), as shown in the insets of (a) and (b). The relative sizes of the light cones and d_0 will remain the same for different fiber diameters $2R_0$ because Eqs. (1a), (8a) and (8b) depend on R_0 linearly.

3.1. Inscription in the 80 μm-diameter fiber

The left-hand side panels of Figs. 4(a) and 4(b) show some representative optical microscopy images of the FS laser induced modification in the 80 μm-diameter fiber. The plots on the right-hand side of Figs. 4(a) and 4(b) compare the experimental data with the simulations based on Eq. (2) (Fig. 4(a)) and Eq. (4) (Fig. 4(b)). In these simulations, as well as in the simulations pertinent to the other fibers under consideration, the refractive index of the fiber material n was assumed to be 1.45 (fused silica (SiO_2) at $\lambda = 800$ nm). Figure 4(a) represents the case when there was no phase mask in the beam path, whereas Fig. 4(b) represents the case when the 1st-order mask (i.e., $\Lambda^{(1)} = 1.07$ μm) was inserted in the beam path.

Point O_1 in the plots indicates at which source distance s the image distance i is equal to R_0 (i.e., 40 μm). The respective value of s_{R_0} is $-R_0$ if there is no phase mask in the beam path and is given by Eq. (6) if a phase mask with a period of Λ (i.e., $\Lambda^{(1)}$) is in the beam path. Point O_2 indicates at which source distance s the image distance i is equal to $2R_0$ (i.e., 80 μm) and material modification can thus be induced at the back surface of the fiber. This source distance s_{2R_0} is negative for $n = 1.45$ and if there is no phase mask in the beam path, is given by

$$s_{2R_0} = \frac{2R_0}{n-2} \tag{8a}$$

and by

$$s_{2R_0} = \frac{2R_0\Lambda}{\sqrt{(n\Lambda)^2 - \lambda^2 - 2\sqrt{\Lambda^2 - \lambda^2}}} \tag{8b}$$

if a phase mask with a period of Λ is placed in the beam path. Equations (8a) and (8b) together with the above definitions of points O_1 and O_2 will also be applied to analyze the experimental data on laser-inscription inside the 125 μm- and 400 μm-diameter fibers (see Table 1).

Table 1. Calculated distances s_{R_0}, s_{2R_0}, D_{R_0} and experimentally determined distances D_{R_0}

	80 µm-diameter fiber		125 µm-diameter fiber				400 µm-diameter fiber	
	No PM	1^{st}-order PM	No PM	3^{rd}-order PM	2^{nd}-order PM	1^{st}-order PM	No PM	1^{st}-order PM
s_{R_0} (O_1 in Figs. 4-6)	−40 µm	−60 µm Eq. (6)	−62.5 µm	−64.5 µm Eq. (6)	−67 µm Eq. (6)	−94 µm Eq. (6)	−200 µm	−301 µm Eq. (6)
s_{2R_0} (O_2 in Figs. 4-6)	−145 µm Eq. (8a)	−933 µm Eq. (8b)	−227 µm Eq. (8a)	−246 µm Eq. (8b)	−275 µm Eq.(8b)	−1457 µm; Eq. (8b)	−727 µm Eq. (8a)	−4663 µm; Eq. (8b)
D_{R_0} (theory)	64 µm Eq. (1)	63 µm Eq. (7)	101 µm Eq. (1)	99 µm Eq. (7)	97 µm Eq. (7)	99 µm Eq. (7)	322 µm Eq. (1)	316 µm Eq. (7)
D_{R_0} (experiment)	62 ± 5 µm	64 ± 3 µm	95 ± 3 µm	96 µm	96 µm	100 ± 3 µm	300 ± 7 µm	320 ± 6 µm

The data presented in the plot of Fig. 4(a) was collected on 4 samples. Some source distances s were the same for the 4 samples and the respective image distances i represent averaged values with a standard deviation of 7 µm. Some datapoints represent non-averaged values. The experimentally measured distance D_{R_0} was 62 ± 5 µm, whereas the predicted value is ≈64 µm (see Eq. (1)). The laser power in the unexpanded FS laser beam was 300 mW if measured in front of L. The sample presented in the optical microscopy image of Fig. 4(a) was prepared using linear polarization of the FS beam aligned along the x-axis.

The data presented in the plot of Fig. 4(b) was collected on 2 samples. The source distances s were the same for the 2 samples and the respective image distances i represent averaged values with a standard deviation of 5 µm. The experimentally measured distance D_{R_0} was 64 ± 3 µm, whereas the predicted value (see Eq. (7)) is ≈63 µm. The laser power in the expanded FS laser beam was 480 mW if measured in front of L. The sample presented in the optical microscopy image of Fig. 4(b) was prepared using linear polarization of the FS beam aligned along the y-axis.

3.2. Inscription in the 125 µm-diameter fiber

As in the previous case of Fig. 4, the left-hand side panels of Figs. 5(a)–5(d) show optical microscopy images of the FS laser induced modification, whereas the plots on the right-hand side of Figs. 5(a)–5(d) compare the experimental data with the simulated data. The simulations are based on Eq. (2) for Fig. 5(a) and on Eq. (4) for Figs. 5(b)–5(d). The data in Fig. 5(a) pertain to the case when there was no phase mask in the beam path, whereas Figs. 5(b)–5(d) represent the cases when the 3^{rd}-, 2^{nd}- and 1^{st}-order phase mask, respectively, was inserted in the beam path. As it was mentioned earlier, the period of the 3^{rd}-, 2^{nd}- and 1^{st}-order phase mask is $\Lambda^{(3)}$ (i.e., 3.21 µm), $\Lambda^{(2)}$ (i.e., 2.14 µm) and $\Lambda^{(1)}$ (i.e., 1.07 µm), respectively.

The data presented in the plot of Fig. 5(a) was collected on 5 samples of the 125 µm-diameter fiber. Similar to Fig. 4(a), some i-datapoints represent non-averaged values but the majority of the i-datapoints are averaged values with a standard deviation of 4 µm. The experimentally measured distance D_{R_0} was 95 ± 3 µm, whereas the predicted value is ≈101 µm (see Eq. (1)). The laser power in the unexpanded FS laser beam was 300 mW if measured in front of L. The sample presented in the optical microscopy image of Fig. 5(a) was prepared using linear polarization of the FS beam aligned along the x-axis.

The data presented in the plot of Fig. 5(b) was collected on 1 sample. The experimentally measured distance D_{R_0} was 96 µm, whereas the predicted value is ≈99 µm (see Eq. (7)). The data presented in the plot of Fig. 5(c) was also collected on 1 sample. In this case, the experimentally measured distance D_{R_0} was also 96 µm, whereas the predicted value is ≈97 µm (see Eq. (7)). In the above two experiments, the laser power in the expanded FS laser beam was 620 mW if measured in front of L and the linear polarization was aligned along the x-axis. The laser power was higher in this case because the diffraction efficiency of the e-beam written 2nd- and 3rd-order phase mask is lower than that of the 1st-order holographic phase mask

The data presented in the plot of Fig. 5(d) was collected on 5 samples. Again, some *i*-datapoints represent non-averaged values and but the majority of the *i*-datapoints are averaged values with a standard deviation of 5 µm. The experimentally measured distance D_{R_0} was 100 ± 3 µm, whereas the predicted value is ≈99 µm (see Eq. (7)). The laser power in the unexpanded FS laser beam was 480 mW if measured in front of L. The sample presented in the optical microscopy image of Fig. 5(c) was prepared using linear polarization aligned along the *y*-axis.

3.3. Inscription in the 400 µm- diameter fiber

The results on FS laser inscription inside the 400 µm-diameter fiber are presented in Figs. 6(a) and 6(b). As before, the simulations are based on Eq. (2) for Fig. 6(a) and on Eq. (4) for Fig. 6(b). The data in Fig. 6(a) and 6(b) respectively relate to the cases when there was no phase mask in the beam path and the 1st-order phase mask ($\Lambda^{(1)}$ =1.07 µm) was placed in the beam path.

The data presented in the plot of Fig. 6(a) was collected on 2 samples. The majority of the *i*-datapoints are averaged values with a standard deviation of 7 µm. The experimentally measured distance D_{R_0} was 305 ± 7 µm, whereas the predicted value is ≈322 µm (see Eq. (1)). The laser power in the unexpanded FS laser beam was 300 mW if measured in front of L. The sample shown in the optical microscopy image of Fig. 6(a) was prepared using linear polarization aligned along the *x*-axis.

The data presented in the plot of Fig. 6(b) was collected on 3 samples. The majority of the *i*-datapoints are averaged values with a standard deviation of 6 µm. The experimentally measured distance D_{R_0} was 320 ± 6 µm, whereas the predicted value is ≈316 µm (see Eq. (7)). The laser power in the unexpanded FS laser beam was 480 mW if measured in front of L. The sample shown in the optical microscopy image of Fig. 6(b) was prepared using linear polarization aligned along the *x*-axis.

Table 1 lists the calculated distances s_{R_0}, s_{2R_0}, D_{R_0} and experimentally determined distances D_{R_0} that correspond to laser inscription without a phase mask and laser inscription using the 3rd-, 2nd- and 1st-order phase mask.

4. Discussion

The underlying assumption of this work is that a laser focus can be produced within the fiber (F). According to the geometrical optics approach used in this work, it can always be done by choosing s between 0 and s_{2R_0}, which is given by either Eq. (8b) or Eq. (8a) depending on whether there is a phase mask is in the beam path or not, respectively. The source and its image are treated as mathematical lines. Namely, the source is the single focal line produced by the cylindrical lens (L) if there is no phase mask (M) in the beam path and is represented by the overlapping focal lines of the ±1 diffraction orders if a phase mask is in the beam path (see Fig. 2(a)).

In reality, the output circular FS laser beam (B) is a circular Gaussian beam and after the cylindrical lens it becomes an elliptical Gaussian beam stretched along the *x*-axis. The dimensions of the source in the *yz*-plane are now finite and defined along the *y*-axis by its waist size and along the *z*-axis by its Rayleigh range ρ, which is a quadratic function of the waist size. It may be noted that at a distance ρ along the beam propagation direction, if measured from the position of the waist, the width of the beam increases by a factor of $\sqrt{2}$. The Rayleigh range ρ of the focused FS beam can be expressed in terms of the effective numerical aperture (NA) of the cylindrical lens as $\rho = \lambda/(\pi \mathrm{NA}^2)$.

The authors of Ref. [22] considered the case when the phase mask is removed from the optical path and showed that the ability to position the beam waist of a Gaussian beam focused by a cylindrical lens within a fiber depends on ρ, n and R_0. For a fiber with $R_0 = 62.5$ µm and $n = 1.457$ the beam waist is always outside the fiber for $\rho/R_0 > 3$, while the beam waist can be placed within the fiber at any distance from its front surface for $\rho/R_0 < 1.1$. This implies that NA of the focusing cylindrical lens in the "mask-less" case should exceed a certain value in order to satisfy the latter condition. In the "mask-less" case, the above condition was always fulfilled in our experiments as the effective NA of the cylindrical lens was 0.23, which translates into $\rho \approx 5$ µm or $\rho/R_0 \ll 1.1$ for all the fibers tested.

When a phase mask is placed in the beam path, the situation becomes quite different. In the geometrical optics approximation, a focus can be produced within the fiber even in parallel incident rays if the Bravais refractive index $n_B(\theta_1) \geq 2$ [30]. It may be recalled in this connection that in the "mask-less" case the fiber focuses parallel incident rays behind its back surface at a distance given by Eq. (1a). This also suggests a Gaussian-beam analysis of the problem in the presence of a small-period mask (i.e., large $n_B(\theta_1)$), which has not been done yet, would lead to significantly different ρ/R_0-ratios in terms of the ability to produce a focus at the fiber core or within the fiber. For reference, the Bravais refractive index for the 1st-order phase mask used in our experiments, $n_B(\theta_1^{(1)})$, is ≈1.87 and the fiber therefore focuses parallel incident rays into a caustic lying just behind its back surface (see Fig. 3 of Ref. [30]).

4.1. Inscription without a phase mask

The main purpose of the experiments without a phase mask was to check whether the most basic geometrical optics formalism (see Eq. (2)) can adequately describe data obtained under our experimental conditions. More specifically, we looked i) at how accurately Eq. (2) could predict the image position i (i.e., the position of the resultant light-induced material modification) as a function of s and ii) how the shape and type (i.e., Type I versus Type II) of the material modification change with i under the same laser-inscription parameters. The pertinent results, which are visualized in Figs. 4(a), 5(a), 6(a), can be summarized as follows. The experimentally determined distance by which the cylindrical lens should be translated along the z-axis from the initial alignment point to the point where the laser focus reaches the fiber core (i.e., distance D_{R_0}; Eq. (1)) is close to its theoretical value for all the fibers tested. The translation distance of the cylindrical lens along the z-axis from the initial alignment point to the point when the laser focus reaches the front surface of the fiber (i.e., the front focal length (FFL) of the fiber) is therefore also known with a high accuracy – to within a few micrometers. After the laser focus has been placed at the front surface of the fiber ($s = 0; i = 0$), the position of the on-axis (i.e., $y = 0$) material modification can be obtained from Eq. (2), also to within a few micrometers. A much more involved ray tracing is required in order to predict how the position of the modification changes when the lens is scanned along the y-axis at a fixed s (e.g., Fig. 4(a)). Another observation is that the type of material modification changes as the laser focus is moved within the fiber from the front to back surface. The transition from Type I modification to Type II modification clearly indicates that the light intensity in the focused FS pulses is higher in the back halves of the fibers. This effect is mainly due to pulse focusing by the fiber and, in the "mask-less" case, can be relatively easily analyzed using the standard formalism of Gaussian-beam optics [22]. Specifically, using the ray-transfer matrix for a cylindrical air-fiber boundary it can be shown that the Rayleigh range of the FS beam is larger in the surrounding air than inside the fiber and, correspondingly, the beam waist is smaller inside the fiber than in the surrounding air.

The above experiments are important from two points of view. Firstly, the 0 diffraction order of every phase mask contains a certain portion of the incident laser power. This portion can range from ≈2% to ≈30% depending on the phase mask design and FS pulse parameters. The simple formalism introduced for the "mask-less" case allows one to analyze the behavior of the focused 0 diffraction order within the fiber, which is directly relevant to FBG inscription through protective polymer coatings. Secondly, the actual "mask-less" inscription with a cylindrical lens only can be used to produce high-quality regions of Type I modification inside optical fibers. The optical images in Figs. 4(a), 5(a), 6(a), which were obtained in transmitted light, demonstrate that such Type I-structures guide light and thus may be used in in-fiber micro-photonic components.

4.2. Inscription using a phase mask

This case represents the classical PM-technique which is widely used for FBG inscription. The focusing effect introduced by the fiber has never been analyzed in the literature in terms of diagonally incident diffracted light. A rigorous treatment of the problem is very difficult because it requires i) calculating the temporal and spatial distribution of the FS pulse's electric field in the focal volume formed by the combination of a cylindrical lens and a phase mask and after that ii) solving a vectorial diffraction problem at the highly curved cylindrical surface of the fiber for the case of diagonally incident electromagnetic radiation. The treatment should also include the residual aberrations of the cylindrical lens and the beam quality factor of the FS laser. Under some high-power inscription conditions, equations governing the propagation of FS laser pulses in the fiber material should include nonlinear terms. A thorough analysis of nonlinear pulse propagation in different isotropic media, such as gases and transparent isotropic solids, can be found in Ref. [41].

Accurate numerical simulations that would take into account all of the aforementioned aspects are extremely difficult. However, as we have shown in this work and also in Refs. [18,19,20,21,37], simple analytic expressions based on geometrical optics provide insight into the nature of several observable effects. We also note that self-focusing can be neglected in the current analysis. Indeed, in Ref. [42] we provided evidence that morphologically similar structures can be produced with 1 mJ 80 fs pulses and 1 mJ 350 fs pulses, i.e., at a roughly 4 times lower intensity. Based on that, we came to a conclusion that the intensity distribution rather than the intensity magnitude is responsible for the modification morphology and self-focusing is not the dominant effect to define the intensity distribution inside the fiber under our experimental conditions. In this work we used the same laser-writing setup as in Ref. [42] but the pulse energy was significantly lower (i.e., 0.48 mJ and 0.62 mJ), which should have reduced the impact of nonlinear optical effects even further. The above remarks also apply to the "mask-less" inscription discussed earlier.

Figures 4(b), 5(b)-(d) and 6(b) show experimental evidence that our semi-quantitative formalism can be used to i) find the position of material modification as a function of s and ii) predict the type, shape and size of material modification as a function of s when the PM-technique is used.

As in the "mask-less" case, the experimentally determined distance D_{R_0} (see Eq. (7)) agrees with its theoretical value for all the fibers tested. As a result, the front focal length (FFL) of the fiber for angled irradiation can also be accurately predicted using Eq. (1a), provided that n_{B} is used instead of n. After the laser focus has been moved by FFL and thus placed at the front surface of the fiber ($s = 0; i = 0$), the position of the on-axis (i.e., $y = 0$) material modification can be obtained from Eq. (4).

A summary of the pertinent results is provided below. The image distance i as a function of s approaches its $2R_0$-value progressively slower as the period of the phase mask Λ gets smaller. The strongest dependence of i on s around s_{2R_0} was in the "mask-less" case. When the 3rd- or 2nd-order mask (i.e., $\Lambda^{(3)} = 3.21$ μm and $\Lambda^{(2)} = 2.14$ μm) was used, the inscription could be performed across the whole fiber. With the 1st-order phase mask (i.e., $\Lambda^{(1)} = 1.07$ μm) no visible material modification could be induced inside all the fibers under consideration beyond a certain cutoff value of i, for example $i \approx 115$ μm for the 125 μm-diameter fiber (Fig. 5(d)). The type of material modification changed from Type I to Type II in the case of the 3rd- and 2nd-order mask (Figs. 5(b) and 5(c)) when the laser focus was moved from the front to back surface, similar to what was observed in the experiments without a phase mask. The inscription performed using the 1st-order phase mask was different in this respect as the modification across the fibers was predominantly of Type II. Additionally, the size of the laser-modified regions decreased very rapidly, both along the y-axis and the z-axis, as i approached its cutoff value (Figs. 4(b), 5(d) and 6(b)).

The existence of a well-defined maximum (or cutoff) distance from the fiber's front surface at which material modification cannot be induced using small-period phase masks with large diffraction angles we explain using the following arguments. Firstly, according to Eq. (8b), s_{2R_0} increases rapidly as Λ decreases the other parameters remain fixed. The distance by which the cylindrical lens needs to be moved from the alignment point (point 1 in Figs. 7(a) and (b)) to the point when the focus reaches the back surface fiber (point 2 in Figs. 7(a) and (b)) is nominally given by FFL + $|\mathrm{s}_{2R_0}|$. In order to induce modification near the back surface of the fiber, the cylindrical lens needs to be moved forward many hundreds of micrometers. For example, in the case of the 1st-order phase mask this distance is ≈1462 µm for the 125 µm-diameter fiber (FFL ≈ 5 µm; $|\mathrm{s}_{2R_0}| \approx 1457$ µm). At such a large FFL + $|\mathrm{s}_{2R_0}|$, however, the focused FS beam essentially bypasses the fiber, as it is visualized in Fig. 7(a). This effect will be dramatically reduced for laser-inscription with the 3rd-order phase mask, in which case FFL + $|\mathrm{s}_{2R_0}|$ is ≈281 µm (Fig. 7(b)) for the same 125 µm-diameter fiber. In Figs. 7(a) and 7(b), the movement of the source by the cylindrical lens and the focusing geometry of the FS beam (B) are analyzed in the yz-plane. We note that in this case i) the apparent numerical aperture of the cylindrical lens becomes larger and is given by $(\mathrm{NA}\cdot\Lambda)/\sqrt{\Lambda^2-\lambda^2(1-\mathrm{NA}^2)}$ ($\Lambda = \Lambda^{(1)}$ in Fig. 7(a) and $\Lambda = \Lambda^{(3)}$ in Fig. 7(b)) and ii) the distance between points 1 and 2, d_0, is given by $d_0 = (\mathrm{FFL} + |s_{2R_0}|)\cos\theta_1$, where θ_1 is defined by either $\theta_1^{(1)} = \sin^{-1}\lambda/\Lambda^{(1)}$ or $\theta_1^{(3)} = \sin^{-1}\lambda/\Lambda^{(3)}$.

Laser inscription in the back half of the fiber using the 1st-order phase mask is also complicated by i) the strong polarization dependence of the reflection coefficients at the air-fiber interface for light incident at small grazing angles (i.e., near the "north" and "south" poles of the fiber cross section) and ii) very strong spherical aberration caused by the refraction of marginal rays at the air-fiber interface in the pole regions. All the above effects make the calculation (and even estimation) of light intensity in the focal region near the fiber's back surface very difficult in the case of phase masks with large diffraction angles.

4.3. FBG inscription through protective coatings

Here we would like to emphasize the relevance of the formalism presented in this work for FBG inscription through protective polymer coatings. Generally, a phase mask produces a set of diffraction orders whose diffraction angles are given by $\theta_k = \sin^{-1}\lambda k/\Lambda$, where k is a positive integer satisfying the condition $\lambda k/\Lambda \leq 1$. The material modification (or damage) threshold of the polymer coatings is much lower than that of the silica glass of the fiber. It is important to ensure that the overlapping focal lines of the $\pm k$ $(k \neq 1)$ are sufficiently far away from the coating during the inscription in order not to ablate it. In the case of a 1st-order phase mask, for example, the focal line of the 0 diffraction order should be sufficiently far away from the back surface of the fiber when the overlapping focal lines of the ±1 diffraction orders are inside the fiber's core region.

When the cylindrical lens is translated by $|\Delta z|$ along the z-axis, the focal lines of the $\pm k$ diffraction orders move behind the phase mask by $|\Delta z|\cos\theta_k$. Because phase masks are designed to concentrate the incident laser power in the ±1 diffraction orders, it is natural to take the distance of the focal lines of the ±1 diffraction orders from the phase mask, D_1, as a reference. In this case, the focal lines corresponding to the $\pm k$ $(k \neq 1)$ diffraction orders are located at $(D_1/\cos\theta_1)\cos\theta_k$ from the back surface of the phase mask.

The optimum mask-to-focus distance can be calculated based on the interplay of chromatic, diffraction and aberration effects introduced by the laser-writing setup. The impacts of these effects, especially in the context of tight-focusing geometries and small-period phase masks, were rigorously discussed in Ref. [18]. We showed that there exist two independent sets of phenomena that affect the size and shape of the focal volume after the phase mask. Specifically, these effects include i) spherical aberration caused by the mask substrate, counteracted by conical diffraction occurring at the mask, and ii) angular chromatic dispersion by the phase mask, counteracted by chromatic aberration of the cylindrical focusing lens. Experimental validation of the above effects is presented in Ref. [18], whereas approximate expressions to find the optimum D_1 for a given combination of the laser-inscription parameters can be found in Ref. [43]. Distance D_1 also determines whether the different diffraction orders overlap and a Talbot-like interference pattern is formed as a result or, when the longitudinal walk-off between the diffraction orders is large enough [20], a pure two-beam interference pattern is produced. In any respect, D_1 is a key parameter of the laser-writing setup and its choice significantly affects the ability to perform through-the-coating inscription of FBGs.

After distance D_1 has been selected, Eqs. (2) and (4) allow one to predict where the focal lines of the 0 and $\pm k$ diffraction orders are positioned with respect to the coated fiber. Of course, R_0 in Eqs. (2) and (4) now stands for the radius of the coated fiber, while, in the first approximation, n and n_B can be treated as weighted averages of the refractive indices of the fiber material and the coating.

4.4. Alignment procedure as applied to Gaussian beams

When the alignment procedure (see Section 2.2.) is applied to Gaussian beams, the waist of the input FS beam becomes the source (or the object) for the rod lens represented by the fiber (F; see Fig. 2(b)) and the waist of the output FS beam becomes the image.

According to Ref. [44], a thin-lens equation for Gaussian beams can be written as

$$\frac{1}{s+\rho^2/(s-f)}+\frac{1}{i}=\frac{1}{f}, \tag{9}$$

where ρ is the Rayleigh range of the source, f is given by Eq. (1) (i.e., f is the effective focal length (EFL) of the fiber) and s, i are the source and image distances, respectively. In the context of the alignment procedure, distances s, i and f are positive (the fiber is a positive rod lens; the source and image are real as the source lies in front of the fiber and the image is formed behind the fiber). As before, all the pertinent distances for diffracted beams are measured in the plane that contains the y-axis and is at an angle θ_1 with respect to the yz-plane. Equation (9) shows that when the source waist is one f away from the input side of the fiber, the image waist is also one f away from the fiber – not at infinity. In fact, the maximum achievable distance of the image waist, $i_{\max}$, from the back principal plane of the fiber (P_B in Fig. 2(b)) is given by $i_{\max} = f + f^2/2\rho$, which happens when $s = f + \rho$ [44]. For NA = 0.23 (i.e., our experimental conditions), ρ is nominally ≈5 µm yielding $i_{\max} = 4.8 \times 10^2 \mu$m for the 80 µm-diameter fiber and $i_{\max} = 1.01 \times 10^4 \mu$m for the 400 µm-diameter if there is no mask in the FS beam. Irrespective of the exact values of ρ and f, the above "maximum distance" condition ensures that the half-angle of divergence of the image attains its minimum value, and, as a consequence, the extent of the FS beam behind the image plane becomes the smallest in the vertical plane at a fixed observation distance from the fiber. The observation distance in our experiments was ~10 cm in each case.

As it was mentioned earlier, the focal lines of the 0 and ±1 diffraction orders were placed 300 µm behind the back surfaces of the phase masks by adjusting the position of the cylindrical lens (L). At this distance in the case of the 1^{st}-order phase mask, spherical aberration caused by the mask substrate is compensated by conical diffraction occurring at the mask and, as result, the experimentally measured ρ is the smallest, approximately 5 µm [18]. When focusing is performed through the substrate of the 1^{st}-order mask (i.e., the "mask-less" case) or the 2^{nd}- and 3^{rd}-order masks, the respective focal volumes are distorted by the uncompensated spherical aberration and the apparent ρ's become much larger, in the range of 15-20 µm [18]. As a consequence, the alignment procedure becomes less accurate and the experimentally obtained values of D_{R_0} may be affected by a systematic error caused by the visual interpretation of the images formed in the far zone. Nonetheless, our experiments on ablation of the fiber's front surface confirmed that the alignment procedure remains quite accurate despite the abovementioned issues. Specifically, in order to ablate the front surface of the 125 µm-diameter fiber, the cylindrical lens had to be moved towards the fiber by 7 ± 2 µm from the initial alignment point in the case when the focusing was performed through the 1st-order mask and by 38 ± 3 µm for the focusing through the substrate of the 1st-order mask without intercepting the grooves. These distances are close to the respective nominal FFL's obtained from Eq. (1a), provided that the ordinary refractive index n of the fiber is replaced by its Bravais refractive index $n_{\mathrm{B}}(\theta_1)$ for diagonal illumination. Namely, the FFL is ≈5 µm for the illumination through the 1-st order mask and ≈38 µm for the "mask-less" illumination.

5. Conclusion

Inscription of FBGs using the PM-technique and FS lasers is based on multiphoton absorption. Multiphoton absorption of FS pulses inside transparent media is easily achieved if they are focused sufficiently tightly. The material surrounding the focal volume remains unaffected by the FS pulses passing through it, which nominally allows one to microstructure fibers in a 3-D fashion and also inscribe FBGs through different types of protective coating. In this work, we have proposed a simple and intuitive formalism based on geometrical optics to calculate the position of the light-induced modification inside the fiber as a function of the position of the focusing lens. Our formalism is applicable to all the diffraction orders produced by the phase mask on condition that the inscription is performed in the in-plane manner, i.e., when the axes of the FS beam, the cylindrical lens and the fiber lie in one plane. For the relatively tight focusing geometry used in our work, the agreement between the experimental and modeled data is good for different fiber diameters (i.e., 80 µm, 125 µm and 400 µm) and different diffraction angles (i.e., 0°, $\theta_1^{(3)} \approx 14.4°$ for $\Lambda^{(3)}$, $\theta_1^{(2)} \approx 22°$ for $\Lambda^{(2)}$ and $\theta_1^{(1)} \approx 48.4°$ for $\Lambda^{(1)}$). The fulfillment of the tight-focusing condition is essential as it ensures that that the cylindrical lens produces a well-defined line-shaped focus within the fiber at any distance from its front surface. In this respect, the results of this work are less relevant for FBG inscription with nanosecond excimer lasers in which tight focusing geometries and large diffraction angles are typically not used.

The main conclusion of our studies is that inscription of FBGs using small-period phase masks featuring large diffraction angles (e.g., ≈48.4°) is practically impossible near the back surface of the fiber if the fiber is irradiated from one side. It is a significant limitation of the PM-technique as the reflectivity of FBGs produced with small-period phase masks is much stronger than the reflectivity of FBGs produced with high-order large-period phase masks. In principle, the severe distortion of the laser focus inside the fiber caused by its cylindrical geometry can be removed even for large diffraction angles if the inscription is performed through a glass slip placed on top of the fiber and the refractive indices of the fiber and the slip are index-matched, as it was shown for the point-by-point technique in Refs. [45,46].

The results also show that with high-order phase masks having smaller diffraction angles (e.g., ≈14.4° and ≈22°) material modification can be positioned at any predetermined distance from the fiber's front surface by translating the focusing cylindrical lens along the FS beam propagation direction.

The ability to inscribe an off-axis Bragg grating inside a core of a multi-core fiber or cover the core of a large-core fiber with cross-sectionally stitched Bragg gratings is essential for several sensing and fiber-laser applications [23–29,47]. Traditionally, the inscription in this case is performed using point-by-point, line-by-line, or plane-by-plane writing techniques and is often accompanied by fiber rotation about the fiber axis so that the laser focus could consistently reach different radial zones within the fiber. However, the implementation of these approaches imposes very stringent requirements on the optical setup in terms of precision and mechanical stability. In this respect, if the position of the laser line-shaped focus inside the fiber is a known function of the position of the focusing lens, the remarkable robustness and reproducibility of the PM-technique could offer several advantages over the sequential laser-writing techniques. In this context, our work provides important quantitative information on how accurately FBGs can be positioned inside the fiber by translating the cylindrical focusing lens along the FS beam propagation direction and how the type, shape and size of the modification change with the position of the line-shaped laser focus inside the fiber. The use of the PM-technique together with complimentary diagnostic tools to characterize the intensity distribution inside the fiber, for example, nonlinear photoluminescence microscopy [38], would further facilitate the inscription.

The analytical expressions using the Bravais refractive index presented in our work are also important for through-the-coating inscription of FBGs as they can be used to predict where the focal lines of the different 0 and $\pm k$ diffraction orders are positioned with respect to the coated fiber for a given distance of the focusing lens from the phase mask. This knowledge may allow choosing the pertinent distance parameters in such a way that when the focal lines of the ± 1 diffraction orders are inside the core region of the fiber the focal lines of the other, "parasitic" diffraction order(s) are sufficiently far away from the coating and photoinduced damage of the coating is thus avoided.

Disclosures. The authors declare that there are no conflicts of interest related to this article.

Data availability. Data underlying the results presented in this paper are not publicly available at this time but may be obtained from the authors upon reasonable request.

References

1. A. Othonos, K. Kalli, D. Pureur, *et al.*, *Fibre Bragg gratings* (Springer Berlin Heidelberg, 2006), pp. 189–269.
2. R. Kashyap, *Fiber Bragg gratings* (Elsevier Inc.: Amsterdam, the Netherlands, 2009).
3. K. O. Hill, B. Malo, F. Bilodeau, *et al.*, "Bragg gratings fabricated in monomode photosensitive optical fiber by UV exposure through a phase mask," Appl. Phys. Lett. **62**(10), 1035–1037 (1993).
4. S. Mihailov, C. Smelser, D. Grobnic, *et al.*, "Bragg gratings written in all-SiO2 and Ge-doped core fibers with 800-nm femtosecond radiation and a phase mask," J. Lightwave Technol. **22**(1), 94–100 (2004).
5. A. Dragomir, D. N. Nikogosyan, K. A. Zagorulko, *et al.*, "Inscription of fiber Bragg gratings by ultraviolet femtosecond radiation," Opt. Lett. **28**(22), 2171–2173 (2003).
6. B. Malo, K. O. Hill, F. Bilodeau, *et al.*, "Point-by-point fabrication of micro-Bragg gratings in photosensitive fiber using single excimer pulse refractive index modification techniques," Electron. Lett. **29**(18), 1668–1669 (1993).
7. A. Martinez, M. Dubov, I. Khrushchev, *et al.*, "Direct writing of fibre Bragg gratings by femtosecond laser," Electron. Lett. **40**(19), 1170–1172 (2004).
8. K. Zhou, M. Dubov, C. Mou, *et al.*, "Line-by-line fiber Bragg grating made by femtosecond laser," IEEE Photonics Technol. Lett. **22**(16), 1190–1192 (2010).
9. R. J. Williams, R. G. Krämer, S. Nolte, *et al.*, "Femtosecond direct-writing of low-loss fiber Bragg gratings using a continuous core-scanning technique," Opt. Lett. **38**(11), 1918–1920 (2013).
10. P. Lu, S. J. Mihailov, H. Ding, *et al.*, "Plane-by-plane inscription of grating structures in optical fibers," J. Lightwave Technol. **36**(4), 926–931 (2018).
11. S. J. Mihailov, D. Grobnic, C. Hnatovsky, *et al.*, "Extreme environment sensing using femtosecond laser-inscribed fiber Bragg gratings," Sensors **17**(12), 2909 (2017).
12. J. He, B. Xu, X. Xu, *et al.*, "Review of Femtosecond-Laser-Inscribed Fiber Bragg Gratings: Fabrication Technologies and Sensing Applications," Photonic Sens. **11**(2), 203–226 (2021).
13. P. J. Lemaire, R. M. Atkins, V. Mizrahi, *et al.*, "High pressure H2 loading as a technique for achieving ultrahigh UV photosensitivity, and thermal sensitivity in GeO2 doped optical fibres," Electron. Lett. **29**(13), 1191–1193 (1993).
14. A. Martinez, I. Y. Khrushchev, and I. Bennion, "Direct inscription of Bragg gratings in coated fibers by an infrared femtosecond laser," Opt. Lett. **31**(11), 1603–1605 (2006).
15. S. J. Mihailov, D. Grobnic, and C. W. Smelser, "Efficient grating writing through fibre coating with femtosecond IR radiation and phase mask," Electron. Lett. **43**(8), 442–443 (2007).
16. M. Bernier, F. Trépanier, J. Carrier, *et al.*, "High mechanical strength fiber Bragg gratings made with infrared femtosecond pulses and a phase mask," Opt. Lett. **39**(12), 3646–3649 (2014).
17. D. Grobnic, C. Hnatovsky, and S. J. Mihailov, "Thermally stable type II FBGs written through polyimide coatings of silica-based optical fiber," IEEE Photonics Technol. Lett. **29**(21), 1780–1783 (2017).
18. N. Abdukerim, D. Grobnic, R. Lausten, *et al.*, "Complex diffraction and dispersion effects in femtosecond laser writing of fiber Bragg gratings using the phase mask technique," Opt. Express **27**(22), 32536–32555 (2019).
19. N. Abdukerim, D. Grobnic, C. Hnatovsky, *et al.*, "High-temperature stable fiber Bragg gratings with ultra-strong cladding modes written using the phase mask technique and an infrared femtosecond laser," Opt. Lett. **45**(2), 443–446 (2020).

20. C. Smelser, D. Grobnic, and S. Mihailov, "Generation of pure two-beam interference grating structures in an optical fiber with a femtosecond infrared source and a phase mask," Opt. Lett. **29**(15), 1730–1732 (2004).
21. C. Hnatovsky, D. Grobnic, and S. Mihailov, "Through-the-coating femtosecond laser inscription of very short fiber Bragg gratings for acoustic and high temperature sensing applications," Opt. Express **25**(21), 25435–25446 (2017).
22. J. Thomas, E. Wikszak, T. Clausnitzer, *et al.*, "Inscription of fiber Bragg gratings with femtosecond pulses using a phase mask scanning technique," Appl. Phys. A **86**(2), 153–157 (2006).
23. M. Becker, A. Lorenz, T. Elsmann, *et al.*, "Single-mode multicore fibers with integrated Bragg filters," J. Light. Technol. **34**(19), 4572–4578 (2016).
24. F. Krämer, C. Möller, C. Matzdorf, *et al.*, "Extremely robust femtosecond written fiber Bragg gratings for an ytterbium-doped fiber oscillator with 5 kW output power," Opt. Lett. **45**(6), 1447–1450 (2020).
25. T. Goebel, J. Nold, C. Hupel, *et al.*, "Ultrashort pulse written fiber Bragg gratings as narrowband filters in multicore fibers," Appl. Opt. **60**(19), D43–D51 (2021).
26. S. Pelletier-Ouellet, L. Talbot, A. Mailloux, *et al.*, "Femtosecond inscription of large-area fiber Bragg gratings for high-power cladding pump reflection," Opt. Lett. **47**(19), 4989–4992 (2022).
27. C. Liu, Y. Jiang, J. Li, *et al.*, "Selective fiber Bragg grating inscription in multicore fiber by femtosecond laser and phase mask," Opt. Lett. **47**(16), 4000–4003 (2022).
28. M. Raguse, S. Klein, P. Baer, *et al.*, "Investigations on high-reflective Fiber-Bragg-Gratings in multimode fibers," Opt. Continuum **1**(5), 965–973 (2022).
29. H. Li, B. Yang, M. Wang, *et al.*, "Femtosecond laser fabrication of large-core fiber Bragg gratings for high-power fiber oscillators," APL Photon. **8**(4), 046101 (2023).
30. C. L. Adler, J. A. Lock, B. R. Stone, *et al.*, "High-order interior caustics produced in scattering of a diagonally incident plane wave by a circular cylinder," J. Opt. Soc. Am. A **14**(6), 1305–1315 (1997).
31. P. L. Marston, "Descartes glare points in scattering by icicles: color photographs and a tilted dielectric cylinder model of caustic and glare-point evolution," Appl. Opt. **37**(9), 1551–1556 (1998).
32. C. M. Mount, D. B. Thiessen, and P. L. Marston, "Scattering observations for tilted transparent fibers: evolution of the Airy caustics with cylinder tilt and the caustic merging transition," Appl. Opt. **37**(9), 1534–1539 (1998).
33. R. A. R. Tricker, *Introduction to Meteorological Optics* (American Elsevier, New York, 1970).
34. O. E. Martinez, "Pulse distortions in tilted pulse schemes for ultrashort pulses," Opt. Commun. **59**(3), 229–232 (1986).
35. Z. Bor, B. Racz, G. Szabo, *et al.*, "Femtosecond pulse front tilt caused by angular dispersion," Opt. Eng. **32**(10), 2501–2504 (1993).
36. A. A. Maznev, T. F. Crimmins, and K. A. Nelson, "How to make femtosecond pulses overlap," Opt. Lett. **23**(17), 1378–1380 (1998).
37. N. Abdukerim, D. Grobnic, C. Hnatovsky, *et al.*, "Through-the-coating writing of tilted fiber Bragg gratings with the phase mask technique," Opt. Express **27**(26), 38259–38269 (2019).
38. C. Hnatovsky, D. Grobnic, and S. Mihailov, "Nonlinear photoluminescence imaging applied to femtosecond laser manufacturing of fiber Bragg gratings," Opt. Express **25**(13), 14247–14259 (2017).
39. C. W. Smelser, S. J. Mihailov, and D. Grobnic, "Formation of Type I-IR and Type II-IR gratings with an ultrafast IR laser and a phase mask," Opt. Express **13**(14), 5377–5386 (2005).
40. C. Hnatovsky, D. Grobnic, D. Coulas, *et al.*, "Self-organized nanostructure formation during femtosecond-laser inscription of fiber Bragg gratings," Opt. Lett. **42**(3), 399–402 (2017).
41. A. Couairon and A. Mysyrowicz, "Femtosecond filamentation in transparent media," Phys. Rep. **441**(2-4), 47–189 (2007).
42. C. Hnatovsky, K. Silva, N. Abdukerim, *et al.*, "Nanoscale morphology and thermal properties of low insertion loss fiber Bragg gratings produced using the phase mask technique and a single femtosecond laser pulse," Opt. Express **30**(26), 47361–47374 (2022).
43. S. J. Mihailov, C. Hnatovsky, N. Abdukerim, *et al.*, "Ultrafast laser processing of optical fibers for sensing applications," Sensors **21**(4), 1447 (2021).
44. S. A. Self, "Focusing of Spherical Gaussian Beams," Appl. Opt. **22**(5), 658–661 (1983).
45. Y. Lai, K. Zhou, L. Zhang, *et al.*, "Microchannels in conventional single-mode fibers," Opt. Lett. **31**(17), 2559–2561 (2006).
46. K. Zhou, Y. Lai, X. Chen, *et al.*, "A refractometer based on a micro-slot in a fiber Bragg grating formed by chemically assisted femtosecond laser processing," Opt. Express **15**(24), 15848–15853 (2007).
47. A. Wolf, A. Dostovalov, K. Bronnikov, *et al.*, "Advances in femtosecond laser direct writing of fiber Bragg gratings in multicore fibers: technology, sensor and laser applications," Opto-Electron. Adv. **5**(4), 210055 (2022).